Draft version May 13, 2020
Typeset using LaTeX default style in AASTeX63

Kinematics of the Magellanic Stream and Implications for its Ionization*

Andrew J. Fox,[1] Elaine M. Frazer,[2] Joss Bland-Hawthorn,[3,4] Bart P. Wakker,[5] Kathleen A. Barger,[6] and Philipp Richter[7]

[1] *AURA for ESA, Space Telescope Science Institute, 3700 San Martin Drive, Baltimore, MD 21218*
[2] *Space Telescope Science Institute, 3700 San Martin Drive, Baltimore, MD 21218*
[3] *Sydney Institute for Astronomy, School of Physics A28, University of Sydney, NSW 2006, Australia*
[4] *ARC Centre of Excellence for All Sky Astrophysics in Three Dimensions (ASTRO-3D), Sydney, Australia*
[5] *Department of Astronomy, University of Wisconsin-Madison, 475 N. Charter St., Madison, WI 53706*
[6] *Department of Physics and Astronomy, Texas Christian University, TCU Box 298840, Fort Worth, TX 76129*
[7] *Institut für Physik und Astronomie, Universität Potsdam, Haus 28, Karl-Liebknecht-Str. 24/25, D-14476, Potsdam, Germany*

(Received February 4, 2020; Revised May 11, 2020; Accepted May 11, 2020)

Submitted to ApJ

ABSTRACT

The Magellanic Stream and the Leading Arm form a massive, filamentary system of gas clouds surrounding the Large and Small Magellanic Clouds. Here we present a new component-level analysis of their ultraviolet (UV) kinematic properties using a sample of 31 sightlines through the Magellanic System observed with the *Hubble Space Telescope*/Cosmic Origins Spectrograph. Using Voigt profile fits to UV metal-line absorption, we quantify the kinematic differences between the low-ion (Si II and C II), intermediate-ion (Si III), and high-ion (Si IV and C IV) absorption lines and compare the kinematics between the Stream and Leading Arm. We find that the Stream shows generally simple, single-phase kinematics, with statistically indistinguishable b-value distributions for the low-, intermediate-, and high-ion components, all dominated by narrow ($b \lesssim 25\,\mathrm{km\,s^{-1}}$) components that are well aligned in velocity. In contrast, we find tentative evidence that the Leading Arm shows complex, multi-phase kinematics, with broader high ions than low ions. These results suggest that the Stream is photoionized up to C IV by a hard ionizing radiation field. This can be naturally explained by the Seyfert-flare model of Bland-Hawthorn et al. (2013, 2019), in which a burst of ionizing radiation from the Galactic Center photoionized the Stream as it passed below the south Galactic pole. The Seyfert flare is the only known source of radiation that is both powerful enough to explain the Hα intensity of the Stream and hard enough to photoionize Si IV and C IV to the observed levels. The flare's timescale of a few Myr suggests it is the same event that created the giant X-ray/γ-ray Fermi Bubbles at the Galactic Center.

Keywords: ISM: kinematics and dynamics – Magellanic Clouds – Galaxy: halo – Galaxy: evolution – quasars: absorption lines

1. INTRODUCTION

The Milky Way provides an unmatched opportunity to dissect the gas flows around a star-forming spiral galaxy. By combining radio 21 cm emission measurements of neutral gas with ultraviolet (UV) absorption measurements of ionized gas and other tracers, we can build an all-sky picture of the multi-phase halo gas and conduct a spatially-resolved analysis of the baryon cycle. Furthermore, we can compare the location of halo clouds with the positions of dwarf

Corresponding author: Andrew Fox
afox@stsci.edu

* Based on observations made with the NASA/ESA Hubble Space Telescope, obtained from the Data Archive at the Space Telescope Science Institute, which is operated by the Association of Universities for Research in Astronomy, Inc., under NASA contract NAS5-26555. These observations are associated with program 11541, 11632, 11524, 11585, 11598, 11686, 12025, 12029, 12038, 12212, 12248, 12275, 12569, 12604, and 14687.

satellites and known structures in the Galactic disk, such as spiral arms and the giant Fermi Bubbles at the Galactic Center (GC). This additional knowledge makes the Galactic halo an ideal location for studying gas flows and their role in galaxy evolution.

By a considerable margin, the largest and most massive gaseous structure in the Galactic halo is the Magellanic Stream (hereafter the Stream), which together with the Leading Arm (LA) extends over 200 degrees across the sky (Nidever et al. 2010). The Stream is an interwoven tail of filaments stripped out of the Magellanic Clouds and trailing them in their orbit around the Milky Way (see Mathewson et al. 1974; Putman et al. 2003a; Brüns et al. 2005; Nidever et al. 2008; D'Onghia & Fox 2016). Thought to be created by a combination of tidal forces, ram pressure, and halo interactions, the Stream and Leading Arm form a benchmark for dynamical models of the Magellanic System (e.g. Moore & Davis 1994; Mastropietro et al. 2005; Besla et al. 2010; Guglielmo et al. 2014; Hammer et al. 2015; Pardy et al. 2018; Wang et al. 2019; Lucchini et al. 2020) and a probe of many astrophysical processes.

UV absorption-line studies with the spectrographs on board the *Hubble Space Telescope* (*HST*) have led to considerable progress in our knowledge of the Stream's physical and chemical properties (Lu et al. 1994; Gibson et al. 2000; Fox et al. 2010, 2013, 2014; Richter et al. 2013; Kumari et al. 2015; Howk et al. 2017). These studies indicate that the Stream has a dual origin (as also indicated by the H I kinematics; Nidever et al. 2008), with one filament showing LMC-like kinematics and chemical abundances and the other showing SMC-like kinematics and abundances (Fox et al. 2013; Richter et al. 2013). In the LA, only gas with SMC-like abundance patterns has been observed (Fox et al. 2018; Richter et al. 2018), though with considerable variation in metallicity between different regions, implying a complex creation history.

Despite this progress, the *kinematics* of the UV metal-line absorption from the Magellanic Stream and LA have never been addressed in detail. These kinematics contain important information on the phase structure, temperature, and non-thermal motions of the gas in the Stream, and therefore provide clues to its origin and history. In this paper we present the first detailed UV kinematic analysis of the Magellanic System. Our study is partly motivated by the results of Bland-Hawthorn et al. (2013, 2019), who discuss evidence from Hα and UV studies for a GC flare several Myr ago. Such a "Seyfert flare" would have flash-ionized the Stream in the Galactic polar regions directly below the GC, where the flux of escaping ionizing radiation is highest, but not the Leading Arm, which is located in a lower-latitude region shielded from the ionization cone. In the Seyfert-flare scenario, the high ions in the polar regions of the Stream are photoionized by the escaping ionizing radiation, and so we expect them to show similar velocity centroids and line widths as the low ions (a single-phase model). On the other hand, if the high ions in the Stream are produced by collisional ionization via processes such as shocks, conductive interfaces, or turbulent mixing layers, then they should show different kinematics than the low ions (a multi-phase model). Indeed, these collisional processes are often invoked for other high-velocity clouds (HVCs) in the Galactic halo (Sembach et al. 2003; Fox et al. 2004, 2005; Ganguly et al. 2005; Collins et al. 2005).

A comparative kinematic study of the high and low ions and their variation across the Stream therefore has the potential to directly address whether an ionizing flare from the GC occurred. This question is given additional relevance by the compelling evidence that now exists for recent (Myr-timescale) activity at the GC, including the giant γ-ray emitting Fermi Bubbles (Su et al. 2010; Dobler et al. 2010; Ackermann et al. 2014), their counterparts in X-rays (Bland-Hawthorn & Cohen 2003; Miller & Bregman 2016), microwaves (Finkbeiner 2004), and polarized radio emission (Carretti et al. 2013), the presence of smaller-scale ($\approx$400 pc) radio lobes within the Bubbles (Heywood et al. 2019), and the tentative detection of radio jets (Su & Finkbeiner 2012), though see Ackermann et al. (2014). Furthermore, AGN activity on $\sim$Myr timescales has recently been inferred from X-ray studies of M31 (Zhang et al. 2019), suggesting that such processes are common in MW-mass spiral galaxies. Our UV kinematic analysis of the Magellanic Stream brings a new method for gauging the GC activity: assessing its impact on the extended gaseous environment.

This paper is structured as follows. In section 2 we describe the creation of our sample and the data-modeling procedures and present our new Voigt-profile fits to the *HST*/Cosmic Origins Spectrograph (COS) spectra. We analyze the UV kinematics of the Stream and Leading Arm in section 3. We then present a discussion in section 4, where we interpret the kinematics in light of origin models for the Stream and the Leading Arm. We summarize our conclusions in section 5.

2. OBSERVATIONS AND DATA HANDLING

2.1. *The Sample*

To form our sample, we began with the 69 *HST*/COS Magellanic sightlines compiled in Fox et al. (2014, hereafter F14), and added one recently-observed LA sightline from Fox et al. (2018). The F14 sample was defined to include AGN that: (1) lie within 30° from the 21 cm emission of the Magellanic System, as defined using the Morras et al. (2000) H I contours; (2) lie in regions where the Magellanic absorption is at $|v_{\rm LSR}| > 100$ km s^{-1}, to avoid blending with interstellar absorption from the Milky Way, and (3) have COS/FUV data with the G130M grating with a signal-to-noise (S/N) ratio of $\gtrsim 5$ per resolution element at 1250Å. The G130M grating spans the wavelength range ≈1150–1450Å, covering C II λ 1334, Si II λ1260,1190,1193, Si III λ1206, and Si IV λ1393,1402. We also include G160M observations if they exist, covering the wavelength range ≈1405–1775Å and so including the C IV doublet $\lambda\lambda$1548,1550. The design and performance of the COS spectrograph is described in Green et al. (2012).

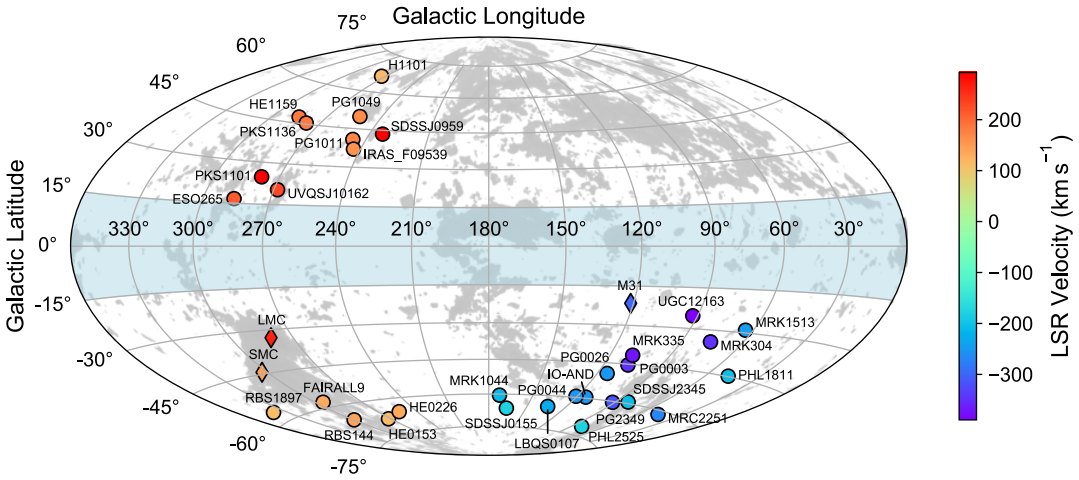

Figure 1. All-sky map in Galactic coordinates showing the location of our COS AGN sightlines with respect to the Stream and Leading Arm. The symbols are color-coded by the LSR velocity of absorption. The grayscale shows the all-sky 21 cm HVC map from Westmeier (2018) based on HI4PI data (HI4PI Collaboration 2016). The locations of the LMC, SMC, and M31 are marked and the Galactic disk is shaded.

We then down-selected the sample to only include sightlines behind the Stream and LA, and not the additional sightlines in F14 passing through the Magellanic Bridge, the LMC halo, and Compact HVCs. This choice was made to keep the analysis focused on two specific spatial regions (Stream and LA). We also removed 7 low-S/N sightlines (S/N<10 per resolution element), since any kinematic information (particularly *b*-values) extracted from these data is unreliable. These are the sightlines toward LBQS0107–0233, RX_J0209.5–0438, SDSS J001224.01–102226.5, SDSS J225738.20+134045.0, SDSS J094331.60+053131.0, ESO 267–G13, and NGC 3125. Together, these steps led to a final sample of 31 Magellanic directions (21 MS and 10 LA). The data can be accessed at MAST via the following link: https://doi.org/10.17909/t9-94ka-p284.

In our earlier work (F14) we drew a distinction between "On-Stream" and "Off-Stream" sightlines, and between "On-Leading Arm" and "Off-Leading Arm" sightlines, based on whether H I 21 cm emission is detected from the Magellanic component in each direction. The reason for the On-Off distinction is that a considerable fraction of the total cross-section of the Magellanic System has an H I column density too low to be detected in 21 cm, and can only be detected in UV absorption (Sembach et al. 2003, F14) or Hα emission (Weiner & Williams 1996; Putman et al. 2003b; Barger et al. 2017). However, in order to preserve a sample size large enough to draw statistically significant conclusions, we do not make the On-Off distinction in this paper, instead leaving our sample as 21 MS directions and 10 LA directions. This means we are covering both On-Stream and Off-Stream directions. The sky distribution of our sample is shown in Figure 1.

Finally, because our sample is defined by an extended spatial region on the sky, some components might have alternative, non-Magellanic origins. A few specific cases are worthy of mention:

(i) Several of our LA components were previously cataloged as tracing other HVC Complexes. These are the components at 80 and 130 km s^{-1} toward PG1011-040, which lies behind Complex WA/WB (Wakker & van Woerden 1991), and the components at 140 and 190 km s^{-1} toward ESO265-G25, which lies behind Complex WD (Wakker & van

Woerden 1991). The association of H1101-232 and PG1049-055 with the LA is also unconfirmed, because they lie off the side of the main H I regions. Despite these complications, we retain these absorbers in the LA sample for two reasons. First, they have high positive LSR velocities broadly consistent with the LA, and so it is possible that they represent detached fragments of the LA regardless of their historical classifications. Second, they are located in the LA region of the halo and are thus exposed to a similar gaseous environment and a similar ionizing radiation field.
(ii) Two absorbers detected in outer-Stream directions (the high-negative-velocity components toward IO And and Mrk 335) might be associated with the halo of M31, since the velocity fields of the Stream and M31 overlap (Lehner et al. 2015, 2020).
Despite the presence of these few ambiguous cases, the good general agreement between the kinematics of our UV sample with the 21 cm kinematics of the Magellanic System (F14) supports our treatment of the sample as Magellanic, and suggests that the number of non-Magellanic components is small.

2.2. *Voigt-Component Fitting*

The COS data presented in this paper were reduced using the customized reduction and alignment steps described in F14 and the appendix of Wakker et al. (2015). We used the Python package *VoigtFit* (Krogager 2018) to perform Voigt-profile fits of the UV metal-line absorption profiles for each sightline in the sample. The transitions under study are Si II λ1260,1190,1193, Si III λ1206, Si IV λ1393,λ1402, C II λ1334, and (when COS G160M data are available) C IV λ1548,1550. These lines were chosen since they are among the strongest UV metal lines detected in HVCs (Lehner et al. 2012; Richter et al. 2017), and they arise from only two elements (C and Si), which simplifies the kinematic analysis. For each metal line, we fit the entire absorption profile, i.e. we include both low-velocity clouds ($|v_{\rm LSR}| < 100$ km s^{-1}; LVCs) and high-velocity ($|v_{\rm LSR}| > 100$ km s^{-1}; HVCs) clouds in the *Voigtfit* model, even though our analysis is focused on the (Magellanic) HVCs. This is because accurately modeling the LVCs enhances the quality of the HVC models by improving the continuum placement. This is particularly true for overlapping clouds that are not well separated in velocity.

Our fitting methodology for each metal line was as follows. First, since the COS/FUV native pixel size is 2.5 km s^{-1} and the spectral resolution is $\approx$15–20 km s^{-1} (FWHM; depending on grating) we rebinned the data by three pixels, so the resulting spectra are Nyquist sampled with $\approx$2 rebinned pixels per resolution element. Second, we ran the *Voigtfit* software using the following inputs: the rebinned data, the spectral resolution of $R = 16000$ (FWHM=18.7 km s^{-1}) for G130M observations and $R = 19000$ (FWHM=15.8 km s^{-1}) for G160M observations), the number of components to fit, the desired size of the fitting region (using a default of $\pm$500 km s^{-1}), and an initial estimate for the redshift, column density, and b-value of each component. Our fitting procedure assumed the COS/FUV line spread function (LSF) was a Gaussian with a full-width at half maximum equal to c/R[1], where c is the speed of light. We took the initial parameter estimates from F14 (Tables 1 and 2) and modified by eye as needed based on our inspection of the data, e.g. to separate a broad component into two narrower components, or to refine the velocity range of Magellanic absorption. Third, we used *Voigtfit* to interactively select continuum regions on either side of the line, to model the continuum either with a linear fit or a spline function, and then to normalize the spectra. Finally, we masked any contaminated (blended) portions of the spectrum, then ran the code to simultaneously fit the components and return the χ^2-minimized values of redshift, column density, and b-value for every component.

Once the line fitting was complete, we classified the absorption components into Galactic (low velocities), Magellanic (high velocities of interest to our analysis), or unrelated HVC (high velocities not of interest). This step made use of the known kinematic structure of the Stream (Nidever et al. 2008) and the velocity integration ranges of Magellanic absorption as listed in F14. However, F14 did not sub-divide the Magellanic absorption into multiple components, as we occasionally did here, so the classifications of which absorbers are Magellanic have been updated in some cases.

We plot the *HST*/COS absorption-line spectra for each sightline in the sample in Figure 2 together with our Voigt-profile fits. Each figure shows a low-ion (Si II or C II), intermediate-ion (Si III), and high-ion (Si IV, C IV) absorption profile, including both the data, the *VoigtFit* model, and dashed vertical lines identifying the Magellanic components. In a small number of cases, only two lines are shown, depending on which lines are covered and detected. The figures illustrate the complex component structure and diversity of the COS absorption profiles. In several LA directions, the differences between the low- and high-ion absorption can be seen visually as velocity centroid offsets and line-width

[1] As our paper was nearing completion, a newer version of *Voigtfit* became available with the ability to handle non-Gaussian LSFs. In Appendix A we quantify the minor effect of using the tabulated non-Gaussian COS LSFs provided by the Space Telescope Science Institute instead of using a Gaussian LSF.

Figure 2. Comparison of low-ion (Si II or C II), intermediate-ion (Si III), and high-ion (Si IV or C IV) absorption profiles for each sightline in the sample. In each panel, normalized flux is plotted against LSR velocity, with the data shown as solid colored lines and the best-fit *Voigtfit* model shown in black. The dashed vertical lines show the velocity centroids of each Magellanic component detected (non-Magellanic and low-significance HVCs are included in the fits but do not have vertical tick marks). Blends are marked with the letter "B", non-Magellanic HVCs are marked with "N", and uncertain (low-significance) HVCs are marked with the letter "U". These lettered components are not included in the analysis.

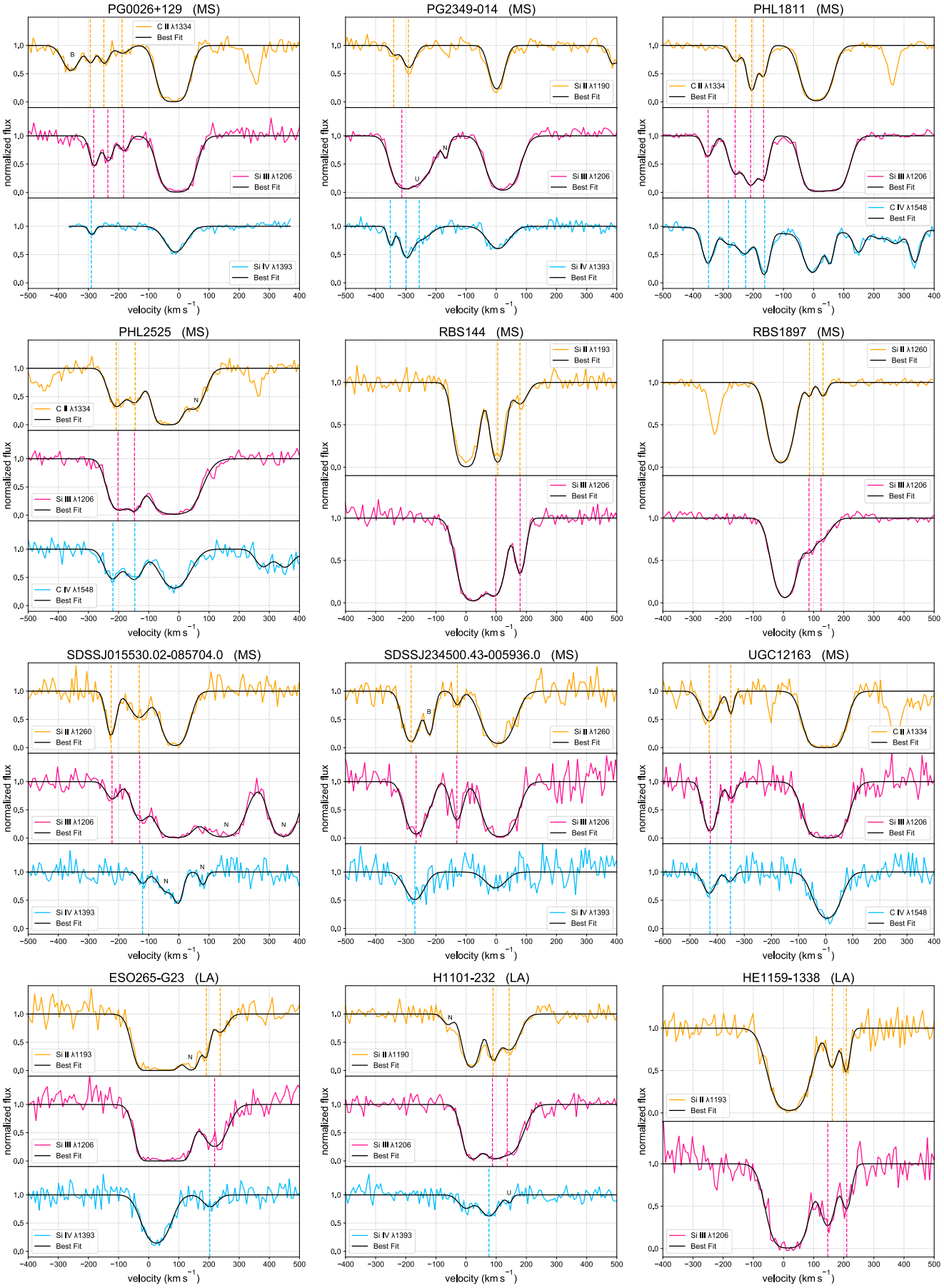

Figure 2. (continued). In some sightlines, only two metal lines are shown, depending on which lines are covered and detected.

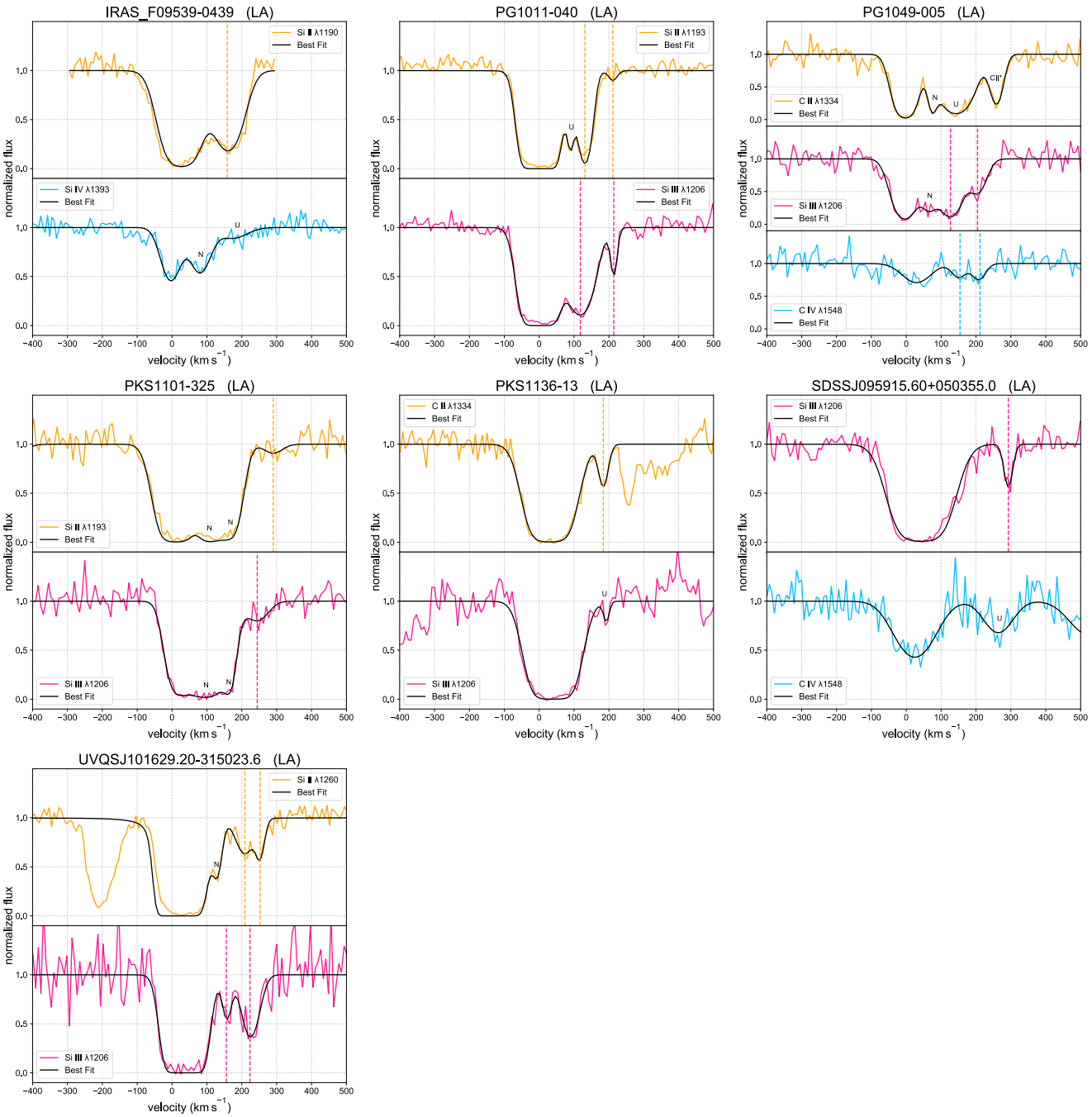

Figure 2. (continued). In some sightlines, only two metal lines are shown, depending on which lines are covered and detected.

differences; we explore these differences quantitatively in section 3. In many directions, multiple components are seen within the Magellanic velocity interval, revealing sub-structure that was not quantified in F14.

3. KINEMATICS

3.1. *Distribution of b-values*

The Doppler b-parameter is a measure of the line width of an absorption component. It encodes information on both the thermal broadening, $b_{\rm th} = \sqrt{(2kT/Am_{\rm H})}$, and the non-thermal broadening, $b_{\rm nt}$, which add together in quadrature to produce the observed line width, $b^2 = b_{\rm th}^2 + b_{\rm nt}^2$. Here A is the atomic number of the absorbing ion, k is the Boltzmann constant, $m_{\rm H}$ is the mass of the hydrogen atom, and T is the temperature. Comparing the b-value distributions of

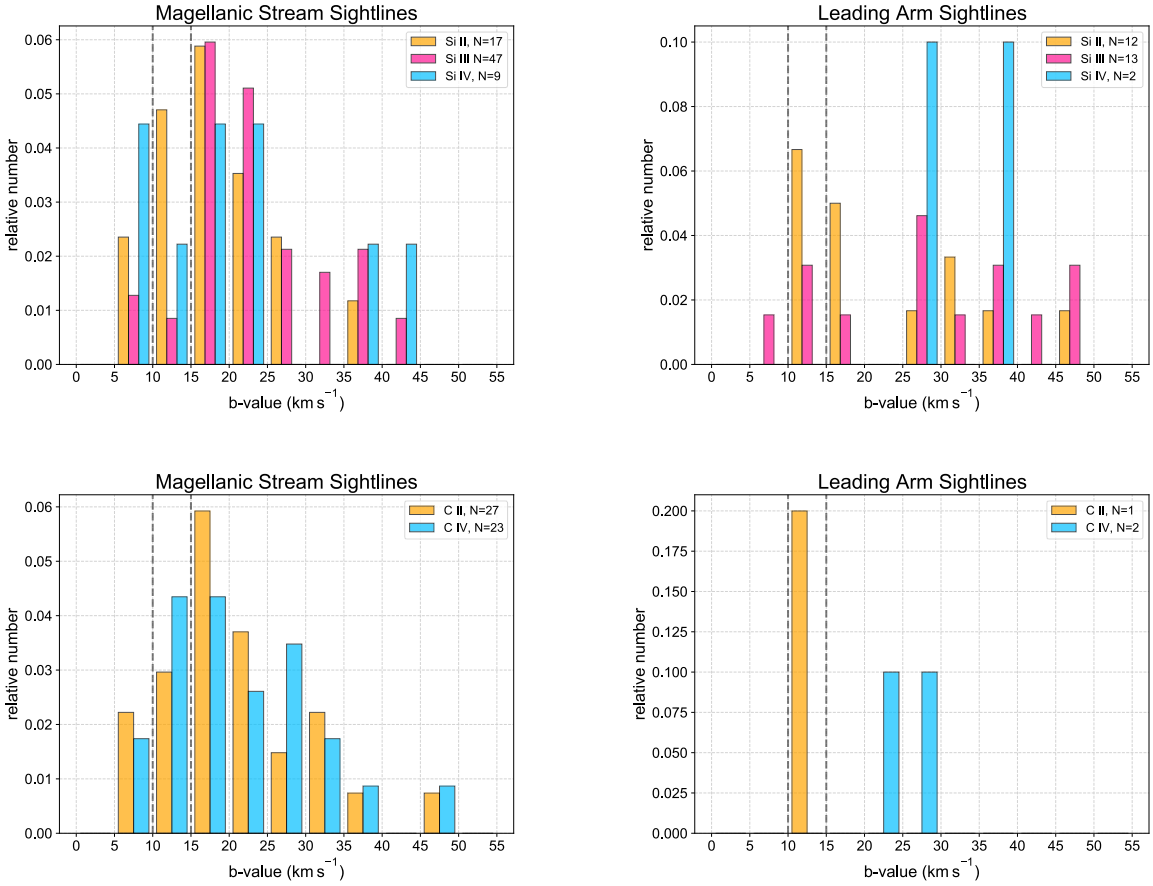

Figure 3. *Top-left*: The distribution of b-values for Si II, Si III, and Si IV components in the Stream sightlines. The histograms are normalized (given as relative number) and the sample size for each ion is indicated in the legend. The two dashed vertical lines shows the COS FUV G160M and G130M instrumental resolution ($b \approx 10\,\mathrm{km\,s^{-1}}$ and $approx 15\,\mathrm{km\,s^{-1}}$). *Top-right*: same but for Si II, Si III, and Si IV in the LA sightlines. *Bottom-left*: same but for the C II and C IV components in the Stream. *Bottom-right*: same but for the C II and C IV components in the LA. There is no statistically significant difference between any of the Stream distributions; the distributions are indistinguishable, both for silicon and carbon.

different ions allows differences in their kinematics to be quantified, which constrains the co-spatiality of the different species.

In Figure 3, we present the b-value distributions for the low-ion (Si II), intermediate-ion (Si III), and high-ion (Si IV) components in the Stream (left) and LA (right). We focus first on all lines of silicon, because they all have the same atomic number, and so their thermal broadening is a function of temperature only (top two panels of Figure 3). We then repeat this for the lines of carbon (C II and C IV; lower two panels of Figure 3). These distributions were formed by combining all the HVC components with Magellanic identifications (either Stream or LA) and then making two "quality-control" cuts to form a reliable sample: (1) we only retain significantly-detected components, defined as those $b > 1.5\sigma_b$; (2) we only retain components with line widths in the range $5 < b < 50\,\mathrm{km\,s^{-1}}$, since a small number of components outside this range were inspected visually and determined to be unreliable, based on saturation or low S/N. The COS/FUV G130M instrumental resolution corresponds to $b \approx 12\,\mathrm{km\,s^{-1}}$, but we choose to retain components down to $5\,\mathrm{km\,s^{-1}}$ since we would otherwise be excluding narrow components from the sample, and although these narrow components are difficult to measure accurately, they are still real. The sample size varies for the different ions, because the data quality (sensitivity) and wavelength coverage varies between systems.

Inspection of Figure 3 shows several interesting features of the b-value distributions in the Stream and LA. In the Stream, the Si II, Si III, and Si IV all have statistically indistinguishable b-value distributions. This is supported by two-sided Kolmogorov-Smirnov (KS) tests between each pair of ions [b(Si II) vs b(Si III), b(Si II) vs b(Si IV), b(Si III)

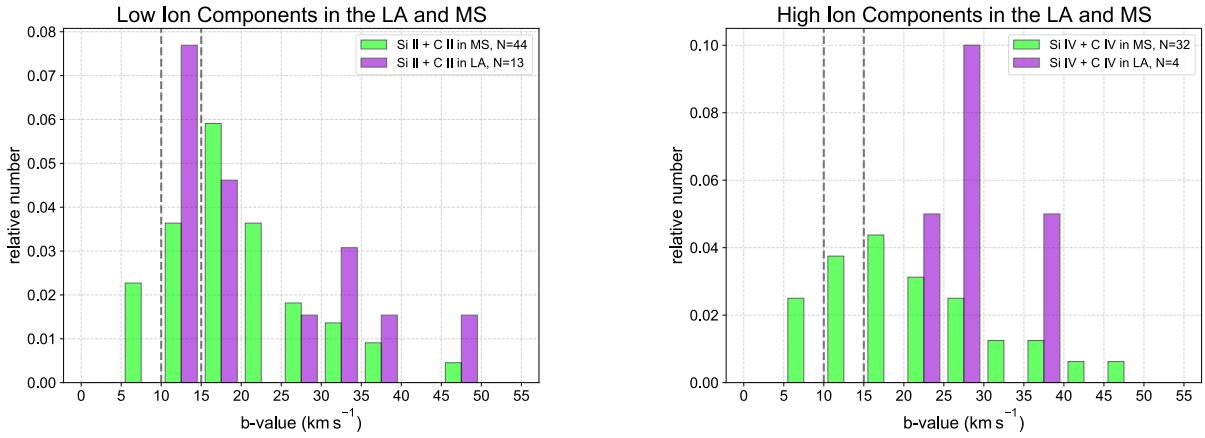

Figure 4. Same as Figure 3 but comparing all *low-ion* components between the Stream and LA in the left panel and all *high-ion* components between the Stream and LA in the right panel. The low-ion b-values distribute similarly in the Stream and LA, with no evidence for any statistical difference. In contrast, a difference in the high-ion b-value distributions exists between the Stream and LA, with the Stream showing mostly narrow ($b < 25\,\mathrm{km\,s^{-1}}$) high-ion components whereas no such narrow components are seen in the LA.

Table 1. Comparison of b-value distributions

Sample	$\langle b$(Si II)$\rangle$	$\langle b$(Si III)$\rangle$	$\langle b$(Si IV)$\rangle$	$\langle b$(C II)$\rangle$	$\langle b$(C IV)$\rangle$	Si III–Si II		Si IV–Si II		Si IV–Si III		C IV–C II	
	($\mathrm{km\,s^{-1}}$)	($\mathrm{km\,s^{-1}}$)	($\mathrm{km\,s^{-1}}$)	($\mathrm{km\,s^{-1}}$)	($\mathrm{km\,s^{-1}}$)	$D_{\rm KS}$	$p_{\rm KS}$	$D_{\rm KS}$	$p_{\rm KS}$	$D_{\rm KS}$	$p_{\rm KS}$	$D_{\rm KS}$	$p_{\rm KS}$
MS	18.7±8.0	23.5±8.6	21.2±11.5	21.2±9.1	21.7±9.6	0.33	0.11	0.16	0.98	0.32	0.33	0.15	0.88
LA	23.5±11.8	29.2±13.3	32.7±3.7	≈14.5[a]	≈25.1[a]	0.28	0.59	0.67	0.33	0.38	0.91	1.00	0.67

NOTE—Columns 2-6 give the mean and standard deviation of the b-value distributions for Si II, Si III, Si IV, and C IV (Figure 3). Columns 6-14 give the D- and p-values from two-sided KS tests comparing the distributions of different ion pairs.

[a]In the LA there is only one C II component and two C IV components, so we do not present a standard deviation.

vs b(Si IV)] which all yield small D statistics with large p-values, indicating that we cannot rule out the null hypothesis that the Si II, Si III, and Si IV b-values are all drawn from the same parent population (see Table 1, which reports the results from the KS tests). The three ions all have a peak near b=20 $\mathrm{km\,s^{-1}}$ and a tail extending to ≈50 $\mathrm{km\,s^{-1}}$, with mean values of 18.7, 23.5, and 21.2 $\mathrm{km\,s^{-1}}$, respectively. The C II and C IV components in the Stream have a mean b-value of 21.2 and 21.7 $\mathrm{km\,s^{-1}}$, respectively (lower panels of Figure 3), i.e. the carbon and silicon lines independently provide the same result that the low-ion and high-ion kinematics agree.

In contrast, for LA directions there is a suggestion that the Si IV tends to be broader than the Si II, with a mean b(Si IV)=32.7 $\mathrm{km\,s^{-1}}$ compared to a mean b(Si II) of 23.5 $\mathrm{km\,s^{-1}}$. However, a two-sided K-S test shows that the significance of this difference is low ($D_{\rm KS}$=0.67, $p_{\rm KS}$=0.33), because of the small sample size. To improve the statistics, in Figure 4 we compare the b-value distributions of *all low ions* (C II and Si II) in the Stream and LA on the left and *all high ions* (C IV and Si IV) in the Stream and LA on the right. The K-S statistics for the Stream vs LA comparison now become $D_{\rm KS}$=0.69, $p_{\rm KS}$=0.04, showing significant evidence for a statistical difference between the two regions.

We visualize the b-value distribution in the Stream and the LA using the maps shown in Figure 5. In these maps the symbol sizes are proportional to the b-value of the Magellanic components, so broader components are shown as larger circles. While the effect is subtle, the tendency for the LA to show broader high-ion components than the Stream is seen in the right-hand map, because larger circles are preferentially found in the upper-left (LA) region of the map.

While our results are statistical, in the sense that they are reported across the ensemble of absorbers in our sample, a few individual spectra illustrate the aligned, narrow nature of the Stream absorbers and the misaligned, broader

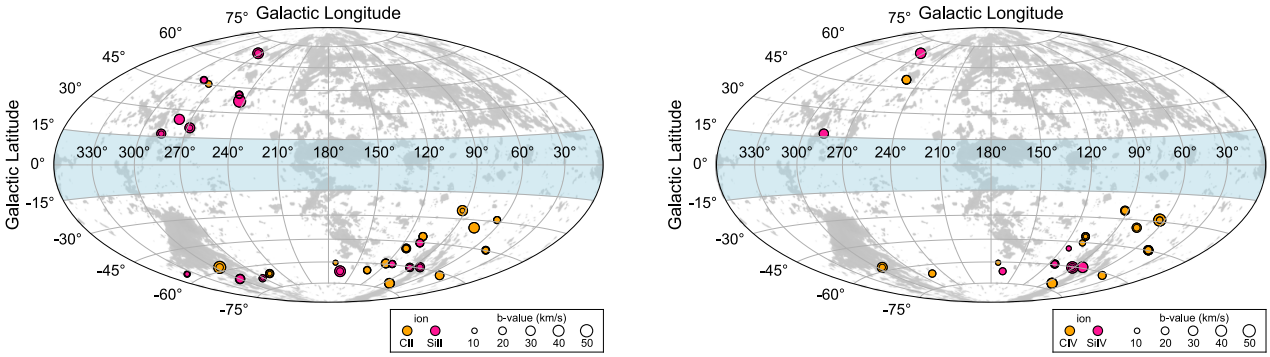

Figure 5. All-sky maps illustrating the Stream and Leading Arm kinematics for the low ions (left panel) and high ions (right panel). Each Magellanic component is shown as a circle, with the size of the circle proportional to the line width (b-value). Concentric circles reflect sightlines with multiple Magellanic components. The grayscale represents the all-sky H I HVC map of Westmeier (2018), as in Figure 1.

nature of the LA absorbers. Narrow high-ion components in the Stream are seen in the spectra of MRC2251–178, PG0026+129, PG2349–014, and MRK1044. In contrast, broad high-ion components are seen in a high fraction of LA directions, including the sightlines to ESO265-G23 and PKS1101–325, and (at lower S/N) toward IRAS F09539–0439, SDSS J095915.60+050355.0 (see Figure 2 and Table 4). Furthermore, narrow C IV and Si IV components have been reported in earlier studies of the Stream and nearby HVCs using the high-resolution E140M grating on STIS in the sightlines to HE0226–4110 (Fox et al. 2005), NGC 7469, and Mrk 335 (both in Fox et al. 2010). Therefore, our result that the Stream has simple kinematics with narrow high-ion components has already been observed in high-resolution data, and so is unlikely to be a COS instrumental broadening effect.

3.2. *Velocity Centroid Alignment*

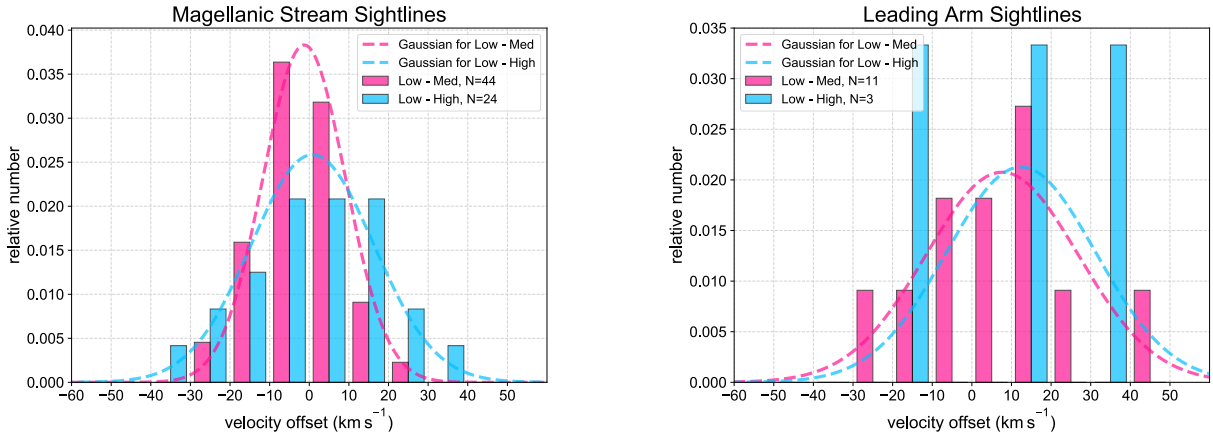

Figure 6. Distribution of velocity centroid offsets for the Stream (left panel) and LA (right panel). In each panel, the distributions are shown for two ion-pairs: high–low (either C IV–C II or Si IV–Si II) or medium–low (either Si III–Si II or Si III–C II). The offsets quantify the difference in line centers between the two components (see subsection 3.2). Both the peak and the width of the offset distribution quantify the degree of alignment of the absorbers.

In addition to the b-values, another kinematic statistic of interest is the velocity centroid offset between any two ions. Single-phase gas clouds will show no centroid offsets between different absorbing species; multi-phase clouds may show significant offsets. A commonly invoked multi-phase scenario is an arrangement where hot, collisionally ionized boundary layers surround cool, photoionized cloud cores. Measurements of the velocity centroid offset can test this scenario and hence diagnose the presence of collisionally ionized gas.

Here we present a new approach for conducting velocity alignment statistics: a nearest-neighbor analysis. In this approach, for each low-ion (Si II) Magellanic component we identify the high-ion (Si IV) component that is closest in velocity. We then measure the velocity centroid offset $\Delta v_0 = v_0$(Si IV)–v_0(Si II) together with its error, which is formed by summing the individual errors on v_0(Si II) and v_0(Si IV) errors in quadrature. We then make a normalized distribution of these offsets and measure the mean value $\langle \Delta v_0 \rangle$ and Gaussian width $\sigma(\Delta v_0)$ of this distribution, excluding any outliers at $\Delta v_0 > 50\,\mathrm{km\,s^{-1}}$, which are likely related to low data quality rather than real offsets. We then repeat this exercise using Si III and Si II, i.e. by analyzing the distribution of v_0(Si III)–v_0(Si II). For single phase clouds, one expects a narrow distribution centered on zero. For multi-phase clouds, one expects a broader distribution that is not necessarily centered on zero. This analysis is illustrated in Figure 6, showing the distribution of velocity offsets for the two pairs of ions, first in the Magellanic Stream (left) and second in the LA (right). We also present a summary of the velocity alignment statistics in Table 2.

Table 2. Velocity Alignment Statistics: Stream vs Leading Arm

Sample	Intermediate–Low		High–Low	
	$\langle \Delta v_0 \rangle$ ($\mathrm{km\,s^{-1}}$)	$\sigma(\Delta v_0)$ ($\mathrm{km\,s^{-1}}$)	$\langle \Delta v_0 \rangle$ ($\mathrm{km\,s^{-1}}$)	$\sigma(\Delta v_0)$ ($\mathrm{km\,s^{-1}}$)
MS	−1.3	10.4	0.8	15.4
LA	7.6	19.2	12.4	18.8

NOTE—This table gives the mean velocity centroid offset, $\langle \Delta v_0 \rangle$, and its standard deviation, $\sigma(\Delta v_0)$, for two pairs of ions: intermediate–low (Si III–Si II or Si III–C II) and high–low (Si IV–Si II and C IV-C II). Small values of $\langle \Delta v_0 \rangle$ and $\sigma(\Delta v_0)$ support single-phase models; larger values support multi-phase models. The absolute velocity scale uncertainty of the COS FUV channel is $\approx$7.5 $\mathrm{km\,s^{-1}}$ (Plesha et al. 2019) for the standard pipeline reduction.

The velocity offset distributions shown in Figure 6 reveal interesting results. In the Stream, the distribution of absolute velocity offsets between Si III and Si II is fairly *narrow*, with a Gaussian width of 10.4 $\mathrm{km\,s^{-1}}$ and a mean value of $-1.3\,\mathrm{km\,s^{-1}}$. The distribution of offsets between Si IV and Si II is slightly broader with a Gaussian width of 15.4 $\mathrm{km\,s^{-1}}$ and a mean value of 0.8 $\mathrm{km\,s^{-1}}$. In contrast, in the Leading Arm the corresponding Si III–Si II offset distribution has a *larger width* of 19.2 $\mathrm{km\,s^{-1}}$ and a larger mean value of 7.6 $\mathrm{km\,s^{-1}}$, and the Si IV–Si II distribution also has a width of 18.8 $\mathrm{km\,s^{-1}}$ (Table 2).These values provide further evidence that the Leading Arm has more kinematic complexity than the Stream, reinforcing the results found from the b-value distributions. The Stream's offset distributions and b-value distributions are consistent with a single phase, whereas the corresponding distributions in the LA support a multi-phase structure.

Note that the velocity offset distributions are related to data quality, because the S/N ratio in a given spectrum impacts the detectability of weak components. For example, a weak Si IV component that is not detected at 3σ significance will not be included in the *VoigtFit* model, even if it is well-aligned with a Si II component; in such a case the nearest-neighbor analysis will instead find an alternative, spurious closest Si IV component to match to the Si II. This would serve to over-estimate the true velocity offset. This effect should be minimized by out choice to exclude outliers with $\Delta v_0 > 50\,\mathrm{km\,s^{-1}}$ from the Gaussian fits to the offset distributions. There were only a handful of such outliers, and visual examination showed they were likely related to low S/N.

In summary, the velocity centroid offsets independently yield the same conclusion as the b-value distributions, namely that the high- and low-ions show simpler kinematics (suggestive of co-spatiality) in the Stream but more complex kinematics (suggestive of non-cospatiality) in the Leading Arm. This dual finding adds to the robustness of the result.

4. DISCUSSION

Our new results constitute the first system-wide analysis of the UV kinematic properties of the Stream and LA. They complement existing studies of the H I 21 cm kinematics (Putman et al. 1998; Kalberla & Haud 2006; For et al. 2013, 2014) and high-resolution UV studies of a few Magellanic sightlines observed with the echelle gratings on *HST*/STIS (Fox et al. 2010; Kumari et al. 2015; Richter et al. 2018). The distributions of b-values and velocity centroids of both

the low and high ions, and their dependence on position within the Magellanic System, provide important information on the phase structure and origin of the ionized gas, and represent important observational constraints for models of the origin and evolution of the Magellanic System. We stress that kinematics alone can determine whether an absorber is multi-phase, even without ionization modeling, because complex kinematics rule out single-phase models.

4.1. *The Photoionized Magellanic Stream*

Our results provide observational evidence that the Magellanic Stream has a simple kinematic phase structure. Single-phase models can explain the Si II, C II, Si III, Si IV, and C IV absorption in the Stream because these ions have indistinguishable b-values distributions (Figure 3) and narrow velocity-centroid-offset distributions (Figure 6). In contrast, we find tentative evidence that the LA is multi-phase, because it shows high-ion components (in C IV and Si IV) that are broader than the low ions (See Figure 3), though more high-S/N data are needed to confirm this in a larger sample. This is suggestive of different physical conditions between the two structures; the high-resolution STIS analysis of the LA presented by Richter et al. (2018) supports the multi-phase picture.

The Stream's simple, single-phase kinematic structure with narrow b-values indicates that it is *photoionized* up to C IV (at least). Since C IV has an ionization potential of creation of 48 eV (to ionize C^{+2} into C^{+3}), this constrains the radiation field incident on the Stream. The finding that the Stream is photoionized up to C IV is an *observational* result, since it is inferred from the UV kinematic data in a model-independent manner.

The Stream's simple UV kinematics are broadly consistent with its H I kinematics; high-resolution 21 cm studies show components with a range of narrow velocity dispersion, almost all $<20\,\mathrm{km\,s^{-1}}$ (Kalberla & Haud 2006; For et al. 2014). However, the widespread presence of O VI in the Stream (an even higher ionization species than C IV; Sembach et al. 2003; Fox et al. 2005) and the occasional detection of molecular gas (Richter et al. 2013) indicate that the Stream overall is multi-phase – our finding of a single phase relates to the UV lines under study only.

The natural question to ask is what is the source of the Stream's photoionization? Candidate sources of ionizing radiation are hot stars in the MW and Magellanic Clouds and the extragalactic UV background (UVB). However, Hα studies (Barger et al. 2017; Bland-Hawthorn et al. 2019) have reported the inability of hot stars or the UVB to explain the bright observed Hα intensity observed along the Stream, and have concluded that an additional source of ionization is required. This is particularly true in the region of the Stream below the South Galactic Pole (SGP), where several clouds with elevated Hα intensity are observed (Putman et al. 2003b), although some of these clouds may be at different distance than the Stream and so may have a non-Magellanic origin.

UV studies of the Stream's ionization (Sembach et al. 2003; Fox et al. 2005, 2010, 2013; Kumari et al. 2015) have also reported the inability of MW and UVB radiation to explain the Stream's observed ionization properties. Detailed *Cloudy* photoionization models that include MW and UVB radiation (but do not include a Seyfert flare) are unable to explain the levels of high-ion absorption observed in UV studies of the Stream. For example, Kumari et al. (2015) reported that the C IV column densities in a Compact HVC off the edge of the main body of the MS are under-predicted by 3 dex by the *Cloudy* models. Fox et al. (2010) reported similar findings in *Cloudy* ionization modeling of two Stream directions. These models account for the non-uniform distribution of escaping radiation from the MW, since they include the enhanced escape fraction of starlight along the Galaxy's minor axis, but even then they cannot explain the observed C IV because the underlying stellar spectrum is not hard enough. A different source of ionizing radiation is required.

4.2. *The Galactic Center Flare*

One potential source of ionizing photons is a Seyfert flare from the GC (Bland-Hawthorn et al. 2013, 2019). In the Seyfert-flare model, the flare photoionized the Stream as it passed underneath the SGP where the flux of escaping ionizing radiation is high, but not the Leading Arm, which lies outside of the ionization cone. The Seyfert-flare model naturally explains the simple, single-phase kinematic structure of the Stream presented in this paper because it is a photoionization model. It is also the only known source of radiation that is powerful enough to photoionize the C IV in the Stream. We now discuss the evidence for this model.

An enhancement in the Stream's Hα intensity in the region below the SGP was first noticed by Putman et al. (2003b) and confirmed by later Hα measurements (Bland-Hawthorn et al. 2013; Barger et al. 2017), which show emission at $\approx$500 milli-Rayleighs below the SGP compared to $\sim$50–100 milli-Rayleighs across the rest of the Stream. Although the interpretation of the Hα enhancement is complicated by the unknown distance to the clouds, the enhancement can be understood as fluorescence induced by a recent GC flare, in which the Milky Way's central supermassive black

hole (SMBH) Sgr A* underwent an outburst several Myr ago (Bland-Hawthorn et al. 2013, 2019), releasing a burst of ionizing radiation and potentially creating the giant X-ray/γ-ray Fermi Bubbles at the same time. This burst would have preferentially ionized the polar regions of the Stream since they lie in the ionization cone directly underneath the GC. The Stream would then recombine and produce the observed Hα enhancement. In this scenario, the Magellanic Stream acts as a screen on which AGN-induced fluorescence occurs.

In contrast to the Hα observations, the C IV/C II ratios in the Stream do not show an unambiguous enhancement below the SGP (Bland-Hawthorn et al. 2019). Instead, they are highest in the MS tip region, farthest from the Magellanic Clouds, where the gas is very fragmented. However, this enhancement may simply reflect the low H I column density N(H I) in that remote portion of the Stream. The C IV/C II ratio depends not only on the shape and intensity of the radiation field, but also on N(H I): gas with low N(H I) is optically thin and so can show a high C IV/C II ratio even in a weak radiation field. Therefore, although the C IV/C II ratio provides important ionization information, it does not offer a clean diagnostic of the incident radiation field, and while the Stream's ion ratios are consistent with the Seyfert flare model, they do not require it.

The *kinematics* of the UV absorbers presented in this paper provide stronger evidence. Clouds photoionized by an ionizing flare will be single-phase and therefore show similar kinematics between low and high ions, with similar line widths and small velocity centroid offsets. Our finding that the Stream has simple, single-phase kinematics is fully consistent with the GC flare model, because the Stream's orbit takes it below the SGP (Gardiner & Nogichi 1996; Besla et al. 2007, 2010) where the flux of escaping ionizing radiation is highest. In contrast, the LA lies closer to the major axis of the disk, where it is shielded from the flare's ionization cone (Bland-Hawthorn et al. 2019), potentially explaining the lack of narrow high-ion components in our LA data. We thus conclude that the Stream's UV kinematics are fully consistent with and provide circumstantial support to the GC flare model, but they do not require it, because other unknown sources of radiation could be present. A follow-up study on the kinematics of HVCs in non-Magellanic directions (particularly in the northern Galactic hemisphere) would be an interesting test of the Seyfert flare model.

The Seyfert flare model is consistent with several independent observed properties of the Stream, including the elevated Hα intensities near the SGP (Putman et al. 2003b; Barger et al. 2017), the UV line ratios (Bland-Hawthorn et al. 2019), and the UV kinematics (this paper). An AGN event such as a Seyfert flare also natural explains many key properties of the Fermi Bubbles, including their spatial extent and energetics (Guo & Mathews 2012; Guo et al. 2012), spatially uniform gamma-ray spectrum (Yang & Ruszkowski 2017), X-ray emission properties (Miller & Bregman 2016), and kinematic age based on entrained cool gas (Fox et al. 2015; Bordoloi et al. 2017). The simplest explanation of these results is that the Seyfert flare was the same event that created the Fermi Bubbles.

4.3. *The Kinematics and Ionization of the Leading Arm*

The complex kinematics of the LA, with broader b-values for Si IV and C IV than for Si II and C II (albeit with a small sample size), indicate the LA is multi-phase (Richter et al. 2018). The LA also shows spatially variable chemical abundances, with oxygen abundances that vary from 4% solar to 30% solar between different cloud regions (Lu et al. 1998; Fox et al. 2018; Richter et al. 2018). These complex, multi-phase conditions provide useful clues to the origin(s) of the LA.

The multi-phase nature of the LA suggests that a different ionization mechanism is required for the high ions in the LA than in the Stream. Collisional processes including shocks (Bland-Hawthorn et al. 2007, 2013; Tepper-García et al. 2015), thermal conduction (Gnat et al. 2010; Borkowski et al. 1990), and turbulent mixing of cool and hot gas (Kwak et al. 2015; Ji et al. 2019) are all expected to be enhanced in the LA because of its proximity to the MW. This proximity leads to an interaction with a much denser external medium than the Stream encounters. Both observations (McClure-Griffiths et al. 2008; Antwi-Danso et al. 2020) and models (Besla et al. 2007; Pardy et al. 2018) indicate that the Leading Arm ($d_{\rm LA}$ $\approx$20 kpc) is much closer to the MW than the Stream is ($d_{\rm MS} > 55$ kpc, and possibly $d_{\rm MS} \approx 75 - 150$ kpc). We suggest that distance (and therefore density of the external medium) is the primary reason why the high-ions appear to be collisionally ionized in the LA but not in the Stream.

The origins of the LA remain unclear. In the classical picture, the LA is formed from tidally stripped Magellanic gas pulled in front of the orbit of the Clouds (e.g. Putman et al. 1998; Besla et al. 2007; Pardy et al. 2018). However, recent work has raised the possibility of contributions from other sources. Parts of the LA, with its highly fragmented H I structure (For et al. 2013), head-tail morphology (Putman et al. 2011), spatially-variable metallicity (Fox et al. 2018; Richter et al. 2018), and stellar counterpart (Price-Whelan et al. 2019; Nidever et al. 2019; Bellazzini et al. 2019) may represent the debris field left over from the accretion and disruption of a forerunner (or forerunners) from

the Magellanic Group (Hammer et al. 2015; Tepper-García et al. 2019) or a stellar cluster in the Galactic halo. Gas condensed from a Magellanic Corona may also contribute to the LA (Lucchini et al. 2020), as may Galactic gas. The LA's complex, multi-phase UV kinematics presented in this paper and in Richter et al. (2018) represent important constraints but by themselves do not allow us to distinguish between origin mechanisms. A full investigation into the physical conditions of the gas in the LA using ionization modeling (and ideally with higher S/N data) would be worthwhile to address these open issues.

5. CONCLUSIONS

Using a sample of 31 *HST*/COS extragalactic sightlines toward background AGN (21 through or near the Magellanic Stream and 10 through or near the Leading Arm), we have presented the first detailed kinematic analysis of the UV metal-line absorption from the Magellanic System. We conducted Voigt-profile fits using the *VoigtFit* software package to characterize the low-ion (Si II, C II), intermediate-ion (Si III) and high-ion (Si IV, C IV) component structure. We derived line centers, line widths, and column densities for each component then calculated the b-value distributions for each ion in both the Stream and the LA, as well as the velocity centroid offset distributions. We used two-sided K-S tests to explore whether any statistically significant differences exist between the kinematics of different ions, and performed a comparative study of the Stream and LA kinematics. Our main results are as follows.

1. In the Stream, the b-values distributions for Si II, Si III, Si IV, C II, and C IV are statistically indistinguishable. All five ions show a distribution with a peak near b=15–20 km s^{-1} and a tail extending to $b \approx 50$ km s^{-1} (compared to an instrumental line width of only $\approx$12 km s^{-1}). Furthermore, the distribution of velocity centroid offsets between intermediate- and low-ion components in the Stream is narrow and centered near zero, with a Gaussian width of only 10.4 km s^{-1}. Both these results indicate the Stream tends to show simple kinematics with a predominantly single-phase structure for the ions under study.

2. In contrast, the Leading Arm b-values for the low-ions and high-ions distribute differently, although the sample size is small. The Si IV b-values (mean of 32.7 km s^{-1}) tend to be broader than the Si II b-values (mean of 23.5 km s^{-1}) and Si III b-values (mean of 29.2 km s^{-1}). The distribution of velocity centroid offsets between Si III and Si II components in the Leading Arm is broader than in the Stream, with a Gaussian width of 19.2 km s^{-1}. Both these results indicate that the Leading Arm has complex kinematics with a multi-phase structure, as found in earlier work (Richter et al. 2018).

3. The finding that the Stream is predominantly single-phase suggests that it is photoionized up to C IV, the most highly ionized species in our dataset. In contrast, there is no evidence for photoionized Si IV and C IV in the Leading Arm, because its Si IV and C IV components tend to be broader and therefore collisionally ionized. The different ionization mechanism for the high ions can be understood in terms of the LA's proximity to the MW ($d_{\rm LA}$ $\approx$20 kpc; McClure-Griffiths et al. 2008; Antwi-Danso et al. 2020), which causes it to interact with a much denser external medium than the Stream does ($d_{\rm MS}$ $\approx$75–150 kpc according to models; Besla et al. 2007; Pardy et al. 2018; Lucchini et al. 2020).

4. The simple, single-phase photoionized nature of the Stream can be naturally explained by the Seyfert flare model (Bland-Hawthorn et al. 2013, 2019), in which a flash of ionizing radiation from the GC photoionizes the Stream as it passes under the south Galactic pole, where the escape fraction is highest. The Seyfert flare is the only known source of radiation that is both powerful enough to explain the Hα intensity of the Stream and hard enough spectrally to photoionize Si IV and C IV to the observed levels.

Acknowledgements. Support for programs 12604 and 14687 was provided by NASA through a grant from the Space Telescope Science Institute, which is operated by the Association of Universities for Research in Astronomy, Inc., under NASA contract NAS5-26555. We are grateful to Jens Krogager for his assistance with installing and implementing *VoigtFit*, to Max Gronke and Adam Ritchey for useful scientific discussions, and to Tobias Westmeier for assistance with HVC maps. We thank the referee for a useful report that improved the quality of the paper.

Facilities: HST (COS)

Software: VoigtFit (Krogager 2018)

REFERENCES

Ackermann, M., Albert, A., Atwood, W., et al. 2014, ApJ, 793, 64

Antwi-Danso, J., Barger, K. A., & Haffner, L. M. 2020, ApJ, 891, 176

Barger, K. A., Madsen, G. J., Fox, A. J., et al. 2017, ApJ, 851, 110

Bellazzini, M., Ibata, R. A., Martin, N. et al. 2019, MNRAS, 490, 2588

Besla, G., Kallivayalil, N., Hernquist, L. et al. 2007, ApJ, 668, 949

Besla, G., Kallivayalil, N., Hernquist, L. et al. 2010, ApJ, 721, L97

Bland-Hawthorn, J. & Cohen, M. 2003, ApJ, 582, 246

Bland-Hawthorn, J., Sutherland, R., Agertz, O., & Moore, B. 2007, ApJL, 670, L109

Bland-Hawthorn, J., Maloney, P., Sutherland, R. S., & Madsen, G. J. 2013, ApJ, 778, 58

Bland-Hawthorn, J., Maloney, P. R., Groves, B., et al. 2019, ApJ, 886, 45

Bordoloi, R., Fox, A. J., Lockman, F. J. 2017, ApJ, 191, 21

Borkowski, K. J., Balbus, S. A., & Fristrom, C. C. 1990, ApJ, 355, 501

Brüns, C, Kerp, J., Staveley Smith, L., et al. 2005, A&A, 432, 45

Carretti, E., Crocker, R. M., Staveley-Smith, L., et al. 2013, Nature, 493, 66

Collins, J. A., Shull, J. M., & Giroux, M. L. 2005, ApJ, 623, 196

Dobler, G., Finkbeiner, D. P., Cholis, I., Slatyer, T., & Weiner, N. 2010, ApJ717, 825

D'Onghia, E., & Fox, A. J. 2016, ARA&A, 54, 363

Finkbeiner, D. P. 2004, ApJ, 614, 186

For, B.-Q., Staveley-Smith, L., & McClure-Griffiths N. M. 2013, ApJ, 764, 74

For, B.-Q., Staveley-Smith, L., Matthews, D., & McClure-Griffiths N. M. 2014, ApJ, 792, 43

Fox, A. J., Savage, B. D., Wakker, B. P., et al. 2004, ApJ, 602, 738

Fox, A. J., Wakker, B. P., Savage, B. D., et al. 2005, ApJ, 630, 332

Fox, A. J., Wakker, B. P., Smoker J. V., et al. 2010, ApJ, 718, 1046

Fox, A. J., Richter, P., Wakker, B. P., et al. 2013, ApJ, 772, 110

Fox, A. J., Wakker, B. P., Barger, K. A., et al. 2014, ApJ, 787, 147

Fox, A. J., Bordoloi, R., Savage, B. D., et al. 2015, ApJL, 799, L7

Fox, A. J., Wakker, B. P., Barger, K. A., et al. 2018, ApJ, 854, 142

Ganguly, R., Sembach, K. R., Tripp, T. M., & Savage, B. D. 2005, ApJ, 157, 251

Gardiner, L. T., & Noguchi, M. 1996, MNRAS, 278, 191

Gibson, B. K., Giroux, M. L., Penton, S. V., et al. 2000, AJ, 120, 1830

Gnat, O., Sternberg, A., McKee, C. F. 2010, ApJ, 718, 1315

Green, J. C., Froning, C. S., Osterman, S., et al. 2012, ApJ, 744, 60

Guglielmo, M., Lewis, G. F., & Bland-Hawthorn, J. 2014 MNRAS, 444, 1759

Guo, F. & Mathews, W. G. 2012, ApJ, 756, 181

Guo, F., Mathews, W. G., Dobler, G., & Oh, S. P. 2012, ApJ, 756, 182

Hammer, F., Yang, Y. B., Flores, H., Puech, M., & Fouquet, S. 2015, ApJ, 813, 110

Heywood, I., Camilo, F., Cotton, W. D., et al. 2019, Nature, 573, 235

HI4PI Collaboration, Ben Bekhti, N., Flöer, L. et al. 2016, A&A, 594, A116

Howk, J. C., Wotta, C. B., Berg, M. A., et al. 2017, ApJ, 846, 141

Ji, S., Oh S. P., & Masterson, P. 2019, MNRAS, 487, 737

Kalberla, P. M. W., & Haud, U. 2006, A&A, 455, 481

Kriss, J., COS Instrument Science Report 2011-01, (STScI: Baltimore)

Krogager, J.-K., preprint (arXiv:1803.01187)

Kumari, N., Fox, A. J., Tumlinson, J. et al. 2015, ApJ, 800, 44

Kwak, K., Shelton, R. L., & Henley, D. B., 2015, ApJ, 812, 111

Lehner, N., Howk, J. C., Thom, C., et al. 2012, MNRAS, 424, 2896

Lehner, N., Howk, J. C., & Wakker, B. P. 2015, ApJ, 804, 79

Lehner, N., Berek, S. C., Howk, J. C, et al. 2020, ApJ, submitted (arXiv:2002.07818)

Lu, L., Savage, B. D., Sembach, K. R. 1994, ApJ, 426, 563

Lu, L., Savage, B. D., Sembach, K. R., et al. 1998, AJ, 115, 162

Lucchini, S., D'Onghia, E, Fox, A. J., et al. 2020, in preparation
Mastropietro, C., Moore, B., Mayer, L, et al. 2005, MNRAS, 363, 509
Mathewson, D. S., Cleary, M. N., & Murray, J. D. 1974, ApJ, 190, 291
McClure-Griffiths, N. M., Staveley-Smith, L., Lockman, F. J., et al. 2008, ApJ, 673, L143
Miller, M. J. & Bregman, J. N. 2016, ApJ, 829, 9
Moore, B. & Davis M. 1994, MNRAS, 270, 209
Morras, R., Bajaja, E., Arnal, E. M., & Pöppel, W. G. L. 2000, A&AS, 142, 25
Nidever, D. L., Majewski, S. R., & Burton, W. B. 2008, ApJ, 679, 432
Nidever, D. L., Majewski, S. R., & Burton, W. B. 2010, ApJ, 723, 1618
Nidever, D. L., Price-Whelan, A., Choi, Y. 2019, et al. ApJ, 887, 115
Pardy, S., D'Onghia, E., & Fox, A. J. 2018, ApJ, 857, 101
Plesha, R., Ake, T., De Rosa, G., Oliveira, C., & Penton, S. 2019, COS Instrument Science Report 2018-25 (Baltimore: STScI)
Price-Whelan, A. M., Nidever, D. L., Choi, Y., et al. 2019, ApJ, 887, 19
Putman, M. E., Gibson, B. K., Staveley-Smith, L., et al. 1998, Nature, 394, 752
Putman, M. E., Staveley-Smith, L., Freeman, K. C., Gibson, B. K., & Barnes, D. G. 2003a, ApJ, 586, 170
Putman, M. E., Bland-Hawthorn, J., Veilleux, S., et al. 2003b, ApJ, 597, 948
Putman, M. E., Saul, D. R., & Mets, E. 2011, MNRAS, 418, 1575
Richter, P., Fox, A. J., Wakker, B. P., et al. 2013, ApJ, 772, 111
Richter, P., Nuza, S. E., Fox, A. J., et al. 2017, A&A, 607, A48
Richter, P., Fox, A. J., Wakker, B. P., et al. 2018, ApJ, 865, 145
Sembach, K. R., Wakker, B. P., Savage, B. D., et al. 2003, ApJS, 146, 165
Su, M., Slatyer, T. R., & Finkbeiner, D. P. 2010, ApJ, 724, 1044
Su, M. & Finkbeiner, D. P. 2012, ApJ, 753, 61
Tepper-García, T., Bland-Hawthorn, J., Sutherland, R. S. 2015, ApJ, 813, 94
Tepper-García, T., Bland-Hawthorn, J., Pawlowski, M. S., Fritz, T. K. 2019, MNRAS, 488, 918
Wakker, B. P., & van Woerden, H. 1991, A&A, 250, 509
Wakker, B. P., Hernandez, A. K., French, D., et al. 2015, ApJ, 814, 40
Wang, J., Hammer, F., Yang, Y. et al. 2019, MNRAS, 486, 5907
Weiner, B. J., & Williams, T. B. 1996, AJ, 111, 1156
Westmeier, T. 2018, MNRAS, 474, 289
Yang, H.-Y. K. & Ruszkowski M. 2017, ApJ, 850, 2
Zhang, S., Wang. Q. D., Foster, A. R., et al. 2019, ApJ, 885, 157

APPENDIX

A. IMPACT OF THE COS LINE SPREAD FUNCTION (LSF)

Table 3. Effect of COS Line Spread Function on *VoigtFit* Output Parameters

Ion	v_0 (km s^{-1})	δb[a] (km s^{-1})	$\delta \log N$[b] (dex)	Note
C II	4	−4.7±1.1	0.13±0.03	*
	82	−5.0±15.5	−0.18±0.30	
	113	2.4±8.4	0.05±0.16	
	155	−2.5±3.9	0.02±0.06	
	205	−1.8±3.2	0.03±0.04	
Si III	3	−6.0±1.1	0.17±0.03	*
	95	−4.8±7.7	−0.09±0.11	
	160	−1.3±4.7	0.04±0.06	
	207	−3.5±2.2	0.09±0.05	
C IV	3	−6.0±1.1	0.17±0.03	*
	95	−4.8±7.7	−0.09±0.11	
	160	−1.3±4.7	0.04±0.06	
	207	−3.5±2.2	0.09±0.05	

NOTE—This table shows the difference in *VoigtFit* output parameters (δb and δ log N) between two sets of models for the absorption components toward the AGN HE0226-4110, one using the tabulated COS LSF and one a Gaussian LSF. The differences are calculated in the sense $\delta b = b_{\rm tabulated} - b_{\rm Gaussian}$ and $\delta \log N = \log N_{\rm tabulated} - \log N_{\rm Gaussian}$. Components with significant ($>2\sigma$) differences are marked with a star in the final column. For all three ions, only the strong low-velocity (Galactic) component shows significant differences in b; the HVC results are not sensitive to the choice of LSF.

[a] Difference in line width, with its error.

[b] Difference in logarithmic column density, with its error.

The *VoigtFit* models presented in this paper were derived assuming the COS/FUV line spread function (LSF) is a Gaussian with a full-width at half maximum FWHM=c/R, where R=16,000 for G130M observations and R=19,000 for G160M observations. When our paper was nearing completion, a newer version of *Voigtfit* became available with the ability to handle non-Gaussian LSFs, allowing the use of the official tabulated COS LSFs, which are slightly non-Gaussian[2]. The COS LSFs have a Gaussian core but include extended wings due to the micro-roughness of the surface of the *HST* primary mirror, which transfers ≈3% of the light from line center to the wings (Kriss 2011).

To quantify the effect of using the tabulated LSFs instead of the Gaussian LSFs, we ran a test case using the AGN HE0226-4110, which was observed at COS Lifetime Position 1 (LP1). This sightline was chosen because of its high S/N COS spectrum, good spectral resolution (LP1 has the highest resolution of all the COS FUV lifetime positions), and the presence of multiple high-velocity metal components of differing line strengths, allowing us to assess the impact of the LSF for both weak and strong lines. We considered three ions: C II, Si III, and C IV, chosen to sample the low ions, intermediate ions, and high ions, respectively. By fitting two sets of *VoigtFit* models, one with the tabulated non-Gaussian LSF and one with the Gaussian LSF, we calculated the difference in the output fit parameters b and log N. The results are summarized in Table 3. For all three ions, the fit parameters obtained with the two LSFs agree

[2] The COS LSFs are available at http://www.stsci.edu/hst/instrumentation/cos/performance/spectral-resolution.

within 2σ for all high-velocity components (including all Magellanic components), but differ for the strong low velocity components, which traces the Galactic ISM. For these low-v components, using the tabulated COS LSF instead of a Gaussian LSF leads to a narrower line width (by 5 $\mathrm{km\,s^{-1}}$) and a larger column density (by 0.15 dex). Therefore for HVCs, there is no evidence for a significant difference in component parameters when using the tabulated LSF versus a Gaussian LSF, and so the kinematic analysis presented in this paper is unaffected by this choice. However, for strong low-velocity absorbers, using the COS LSF has a non-trivial impact on the results.

B. VOIGTFIT RESULTS

In Table 4 we present the full table of *Voigtfit* results for each Magellanic component in our sample (i.e. each HVC with a Stream or Leading Arm identification). We list the velocity centroid (v_0), line width (b) and column density ($\log N$) of each component. The b-value distributions and velocity-centroid-offset distributions analyzed in the paper are based on these raw measurements. We also list the S/N per resolution element measured in the continuum next to each line. Components marked on Figure 2 with the letter "B" (blends), "N" (non-Magellanic HVCs), and "U" (uncertain, low-significance HVCs) are are not included in the table. To be classed as significant, we only include components with $5 < b < 50\,\mathrm{km\,s^{-1}}$ and $b > 1.5\sigma_b$, i.e. reliably measured values.

Table 4. Component Parameters for Magellanic HVCs

Sightline	Sample	Ion	S/N (per resel)	v_0 ($\mathrm{km\ s^{-1}}$)	b ($\mathrm{km\ s^{-1}}$)	$\log N$(ion) (N in $\mathrm{cm^{-2}}$)
FAIRALL9	MS	CII	55	93.9 ± 3.3	18.4 ± 6.7	13.733 ± 0.142
		CII	55	175.8 ± 0.9	48.2 ± 1.7	14.952 ± 0.011
		SiIII	40	105.0 ± 1.2	8.2 ± 3.2	12.698 ± 0.071
		SiIII	40	165.9 ± 1.2	43.3 ± 1.4	13.580 ± 0.012
		CIV	36	126.9 ± 1.8	33.0 ± 4.1	13.624 ± 0.038
		CIV	36	180.9 ± 2.7	13.4 ± 4.5	12.953 ± 0.119
HE0153-4520	MS	SiII	24	91.2 ± 2.4	5.5 ± 8.1	12.808 ± 0.103
		SiII	24	136.2 ± 5.4	17.6 ± 9.9	12.702 ± 0.148
		SiIII	27	117.6 ± 3.3	22.8 ± 3.7	12.923 ± 0.071
		SiIII	27	194.7 ± 0.9	19.4 ± 1.3	12.880 ± 0.020
HE0226-4110	MS	CII	47	84.0 ± 7.5	16.4 ± 10.7	13.221 ± 0.204
		CII	47	113.1 ± 2.7	7.0 ± 6.8	13.345 ± 0.125
		CII	47	154.8 ± 1.5	18.8 ± 3.0	13.881 ± 0.045
		CII	47	204.6 ± 1.5	23.0 ± 2.4	13.960 ± 0.033
		SiIII	42	96.3 ± 3.3	22.3 ± 5.7	12.284 ± 0.080
		SiIII	42	159.3 ± 2.1	24.0 ± 3.8	12.882 ± 0.048
		SiIII	42	206.4 ± 1.5	19.6 ± 1.6	12.972 ± 0.036
		CIV	24	166.2 ± 6.9	18.1 ± 11.6	12.991 ± 0.184
IO-AND	MS	SiII	32	-373.8 ± 2.4	16.2 ± 3.9	12.787 ± 0.064
		SiII	32	-250.2 ± 3.6	14.4 ± 6.3	12.550 ± 0.102
		SiII	32	-179.4 ± 0.9	18.2 ± 1.6	13.270 ± 0.026
		SiIII	38	-375.0 ± 1.5	32.0 ± 2.0	13.017 ± 0.024
		SiIII	38	-243.0 ± 1.5	28.1 ± 2.1	13.118 ± 0.024
		SiIII	38	-182.4 ± 0.9	16.4 ± 1.6	13.083 ± 0.029
		SiIV	59	-169.8 ± 0.6	13.9 ± 1.3	12.878 ± 0.022

Table 4 *continued on next page*

Table 4 *(continued)*

Sightline	Sample	Ion	S/N (per resel)	v_0 (km s^{-1})	b (km s^{-1})	$\log N$(ion) (N in cm^{-2})
		SiIV	59	-229.5 ± 0.6	17.5 ± 0.0	13.119 ± 0.021
		SiIV	59	-385.2 ± 3.6	23.5 ± 5.6	12.367 ± 0.078
LBQS0107-0235	MS	CII	19	-193.8 ± 3.6	14.8 ± 6.7	13.361 ± 0.107
		CII	19	-262.8 ± 8.1	18.6 ± 13.4	13.110 ± 0.200
		SiIII	17	-187.5 ± 7.2	27.8 ± 11.8	12.368 ± 0.138
		SiIII	17	-248.1 ± 2.4	6.0 ± 7.1	12.550 ± 0.301
MRC2251-178	MS	CII	46	-269.1 ± 2.7	24.9 ± 4.3	13.363 ± 0.059
		SiIII	36	-262.8 ± 0.6	19.7 ± 1.1	12.991 ± 0.018
		CIV	38	-269.7 ± 0.6	21.4 ± 1.1	13.799 ± 0.018
MRK1044	MS	CII	26	-211.2 ± 3.9	8.6 ± 9.0	13.008 ± 0.139
		SiIII	28	-209.4 ± 2.7	28.1 ± 4.2	12.581 ± 0.050
		CIV	27	-190.2 ± 3.0	9.0 ± 6.5	12.724 ± 0.125
MRK1513	MS	CII	39	-212.4 ± 3.0	15.0 ± 5.4	13.142 ± 0.086
		CII	39	-275.4 ± 2.1	17.2 ± 3.8	13.351 ± 0.058
		SiIII	32	-210.3 ± 1.2	13.9 ± 2.3	12.549 ± 0.038
		SiIII	32	-277.2 ± 0.9	18.0 ± 1.6	12.799 ± 0.026
		CIV	25	-207.0 ± 5.1	14.0 ± 8.8	12.721 ± 0.171
		CIV	25	-281.4 ± 1.2	14.8 ± 2.7	13.628 ± 0.078
		CIV	25	-310.5 ± 3.6	49.2 ± 2.9	13.981 ± 0.042
MRK304	MS	CII	37	-345.0 ± 2.7	36.5 ± 4.2	13.675 ± 0.042
		SiIII	26	-362.7 ± 3.9	16.6 ± 3.5	12.908 ± 0.129
		SiIII	26	-326.4 ± 4.8	22.4 ± 4.3	13.031 ± 0.099
		CIV	20	-309.3 ± 5.1	28.3 ± 7.2	13.766 ± 0.089
		CIV	20	-355.8 ± 6.3	14.9 ± 9.5	13.258 ± 0.251
MRK335	MS	CII	38	-333.9 ± 2.4	21.9 ± 4.0	13.423 ± 0.055
		CII	38	-411.9 ± 2.7	19.7 ± 4.6	13.308 ± 0.068
		SiIII	36	-250.5 ± 2.4	15.5 ± 4.5	12.280 ± 0.066
		SiIII	36	-297.0 ± 1.8	10.0 ± 4.2	12.407 ± 0.071
		SiIII	36	-339.9 ± 1.8	22.4 ± 3.3	12.758 ± 0.041
		SiIII	36	-412.2 ± 2.1	22.0 ± 3.3	12.519 ± 0.044
		CIV	32	-219.0 ± 1.8	6.8 ± 4.3	12.905 ± 0.077
		CIV	32	-258.0 ± 2.1	17.2 ± 4.6	13.211 ± 0.069
		CIV	32	-306.3 ± 3.3	16.9 ± 5.8	13.261 ± 0.129
		CIV	32	-345.9 ± 9.6	21.0 ± 11.5	12.961 ± 0.232
PG0003+158	MS	SiII	26	-318.6 ± 1.5	18.3 ± 2.8	13.142 ± 0.041
		SiII	26	-380.1 ± 6.3	22.4 ± 10.9	12.591 ± 0.144
		SiIII	23	-244.2 ± 5.7	43.2 ± 8.9	12.635 ± 0.070
		SiIII	23	-326.4 ± 1.5	23.7 ± 2.5	13.055 ± 0.037
		SiIII	23	-394.8 ± 3.3	35.4 ± 4.7	12.902 ± 0.045
		CIV	24	-230.7 ± 1.2	13.2 ± 2.2	13.218 ± 0.042
PG0026+129	MS	CII	22	-188.7 ± 9.0	26.4 ± 15.3	13.224 ± 0.179

Table 4 *continued on next page*

Table 4 *(continued)*

Sightline	Sample	Ion	S/N (per resel)	v_0 (km s^{-1})	b (km s^{-1})	$\log N$(ion) (N in cm^{-2})
		CII	22	-249.0 ± 3.9	18.2 ± 8.2	13.510 ± 0.117
		CII	22	-294.0 ± 3.9	14.1 ± 7.9	13.400 ± 0.136
		SiIII	22	-183.6 ± 4.2	17.6 ± 7.5	12.333 ± 0.107
		SiIII	22	-235.8 ± 2.7	16.2 ± 5.8	12.591 ± 0.080
		SiIII	22	-282.6 ± 2.1	16.4 ± 3.7	12.713 ± 0.056
		SiIV	42	-290.7 ± 2.1	8.8 ± 4.8	12.337 ± 0.078
PG0044+030	MS	CII	11	-214.2 ± 6.0	27.1 ± 9.6	13.755 ± 0.114
		CII	11	-292.8 ± 3.9	23.4 ± 5.8	13.930 ± 0.081
		SiIII	14	-203.7 ± 3.0	14.6 ± 5.0	12.678 ± 0.088
		SiIII	14	-287.4 ± 3.0	37.4 ± 5.0	13.202 ± 0.045
PG2349-014	MS	SiII	24	-291.6 ± 1.8	23.6 ± 2.7	13.421 ± 0.034
		SiII	24	-340.5 ± 3.6	12.5 ± 6.1	12.771 ± 0.114
		SiIII	33	-313.5 ± 3.9	36.0 ± 3.5	13.362 ± 0.089
		SiIV	26	-255.6 ± 23.1	43.6 ± 19.7	13.037 ± 0.278
		SiIV	26	-299.4 ± 2.4	21.5 ± 4.5	13.197 ± 0.182
		SiIV	26	-351.6 ± 1.2	7.8 ± 3.2	12.750 ± 0.050
PHL1811	MS	CII	37	-166.2 ± 1.5	13.9 ± 2.1	13.757 ± 0.038
		CII	37	-205.5 ± 0.9	14.8 ± 1.6	14.099 ± 0.022
		CII	37	-258.3 ± 2.1	20.6 ± 3.7	13.489 ± 0.050
		SiIII	29	-165.9 ± 2.1	16.2 ± 2.0	12.974 ± 0.061
		SiIII	29	-208.8 ± 1.5	22.7 ± 3.6	13.244 ± 0.050
		SiIII	29	-260.4 ± 2.4	23.7 ± 2.6	12.976 ± 0.051
		SiIII	29	-350.1 ± 1.2	18.2 ± 2.1	12.511 ± 0.033
		CIV	41	-162.3 ± 0.6	17.9 ± 1.0	13.941 ± 0.019
		CIV	41	-225.6 ± 4.8	29.4 ± 7.2	13.601 ± 0.110
		CIV	41	-282.3 ± 9.0	28.6 ± 12.9	13.299 ± 0.215
		CIV	41	-348.6 ± 0.9	20.8 ± 1.5	13.730 ± 0.027
PHL2525	MS	CII	22	-145.2 ± 4.8	31.7 ± 8.2	14.079 ± 0.103
		CII	22	-207.9 ± 4.5	30.3 ± 4.5	14.145 ± 0.075
		SiIII	24	-202.2 ± 4.5	35.7 ± 3.9	13.474 ± 0.060
		SiIII	24	-147.3 ± 3.6	23.1 ± 4.0	13.274 ± 0.094
		CIV	20	-219.0 ± 3.9	31.4 ± 5.0	13.738 ± 0.067
		CIV	20	-146.4 ± 3.9	35.1 ± 6.0	13.800 ± 0.063
RBS144	MS	SiII	23	105.0 ± 0.9	22.8 ± 1.1	13.862 ± 0.020
		SiII	23	178.8 ± 4.5	29.6 ± 7.5	12.945 ± 0.081
		SiIII	28	98.4 ± 2.7	31.2 ± 3.0	13.400 ± 0.048
		SiIII	28	179.4 ± 1.2	18.9 ± 1.8	12.899 ± 0.028
RBS1897	MS	SiII	38	86.4 ± 1.8	7.4 ± 4.7	11.941 ± 0.063
		SiII	38	131.4 ± 1.8	13.2 ± 3.6	12.068 ± 0.056
		SiIII	63	84.9 ± 4.5	20.8 ± 7.2	12.441 ± 0.359
		SiIII	63	124.8 ± 19.2	38.7 ± 14.9	12.579 ± 0.282

Table 4 *continued on next page*

Table 4 *(continued)*

Sightline	Sample	Ion	S/N (per resel)	v_0 (km s^{-1})	b (km s^{-1})	$\log N$(ion) (N in cm^{-2})
SDSSJ015530.02-085704.0	MS	SiII	13	-131.7 ± 4.5	38.7 ± 7.5	12.969 ± 0.064
		SiII	13	-225.0 ± 1.5	16.2 ± 2.5	13.073 ± 0.054
		SiIII	18	-130.2 ± 3.9	30.6 ± 5.4	13.072 ± 0.070
		SiIII	18	-222.0 ± 5.1	26.5 ± 8.0	12.539 ± 0.098
		SiIV	16	-120.6 ± 6.9	16.7 ± 12.2	12.611 ± 0.194
SDSSJ234500.43-005936.0	MS	SiII	14	-129.0 ± 5.4	13.1 ± 10.3	12.259 ± 0.166
		SiII	14	-282.6 ± 2.1	27.7 ± 2.9	13.399 ± 0.042
		SiIII	9	-130.8 ± 3.0	22.2 ± 4.2	12.976 ± 0.068
		SiIII	9	-266.1 ± 3.9	34.3 ± 5.3	13.499 ± 0.059
		SiIV	10	-270.0 ± 4.2	37.5 ± 6.2	13.373 ± 0.061
UGC12163	MS	CII	15	-349.8 ± 2.4	7.9 ± 5.7	13.489 ± 0.107
		CII	15	-429.3 ± 3.0	34.8 ± 4.5	14.033 ± 0.047
		SiIII	10	-348.3 ± 5.4	18.0 ± 9.2	12.401 ± 0.137
		SiIII	10	-425.4 ± 1.8	25.7 ± 2.6	13.292 ± 0.044
		CIV	17	-426.9 ± 4.5	27.1 ± 6.7	13.496 ± 0.087
		CIV	17	-351.0 ± 8.7	17.6 ± 14.3	12.933 ± 0.238
ESO265-G23	LA	SiII	12	191.4 ± 2.4	10.1 ± 4.0	13.351 ± 0.091
		SiII	12	237.3 ± 0.0	27.4 ± 10.8	13.043 ± 0.124
		SiIII	11	218.7 ± 3.9	46.5 ± 5.6	13.329 ± 0.043
		SiIV	14	202.5 ± 7.5	29.0 ± 11.5	12.820 ± 0.133
H1101-232	LA	SiII	22	89.4 ± 1.5	17.2 ± 2.4	13.832 ± 0.055
		SiII	22	143.1 ± 3.6	38.1 ± 3.6	13.904 ± 0.043
		SiIII	20	87.6 ± 6.3	27.0 ± 12.3	13.355 ± 0.331
		SiIII	20	136.8 ± 18.0	49.9 ± 10.9	13.563 ± 0.198
		SiIV	21	75.9 ± 4.2	36.4 ± 7.2	13.205 ± 0.064
HE1159-1338	LA	SiII	12	162.3 ± 3.3	18.3 ± 5.8	13.106 ± 0.080
		SiII	12	208.5 ± 2.7	12.2 ± 4.9	13.087 ± 0.078
		SiIII	11	147.3 ± 3.6	29.1 ± 6.2	13.125 ± 0.063
		SiIII	11	210.0 ± 4.2	17.0 ± 6.6	12.710 ± 0.107
IRAS_F09539-0439	LA	SiII	24	158.4 ± 2.1	48.2 ± 2.5	14.221 ± 0.023
PG1011-040	LA	SiII	35	131.4 ± 0.6	19.5 ± 0.7	13.830 ± 0.023
		SiII	35	211.5 ± 2.4	12.8 ± 4.7	12.233 ± 0.078
		SiIII	31	118.2 ± 1.8	42.8 ± 2.2	13.508 ± 0.019
		SiIII	31	214.2 ± 1.2	5.8 ± 3.4	12.572 ± 0.185
PG1049-005	LA	SiIII	15	126.9 ± 6.3	36.9 ± 9.2	13.442 ± 0.095
		SiIII	15	204.6 ± 5.7	30.2 ± 10.9	12.888 ± 0.081
		CIV	13	154.2 ± 12.6	26.0 ± 19.4	13.176 ± 0.260
		CIV	13	211.5 ± 10.5	24.1 ± 14.6	13.224 ± 0.222
PKS1101-325	LA	SiII	20	290.4 ± 14.7	34.1 ± 22.8	12.517 ± 0.237
		SiIII	17	244.5 ± 0.0	38.7 ± 19.9	12.457 ± 0.176
PKS1136-13	LA	CII	22	184.2 ± 1.8	14.5 ± 3.3	13.614 ± 0.054

Table 4 *continued on next page*

Table 4 *(continued)*

Sightline	Sample	Ion	S/N (per resel)	v_0 (km s^{-1})	b (km s^{-1})	$\log N$(ion) (N in cm^{-2})
SDSSJ095915.60+050355.0	LA	SiIII	18	292.8 ± 2.4	12.1 ± 4.3	12.513 ± 0.074
UVQSJ101629.20-315023.6	LA	SiII	24	209.1 ± 5.7	32.5 ± 0.0	12.757 ± 0.098
		SiII	24	252.6 ± 3.0	11.6 ± 5.6	12.472 ± 0.119
		SiIII	8	155.7 ± 5.7	13.7 ± 10.4	12.552 ± 0.166
		SiIII	8	223.5 ± 4.8	29.5 ± 7.6	13.020 ± 0.087